



Agenzia Nazionale per le Nuove Tecnologie,  
l'Energia e lo Sviluppo Economico Sostenibile



*Ministero dello Sviluppo Economico*

## RICERCA DI SISTEMA ELETTRICO

*CERSE-UNIPA RL 1206/2010*

**Modelling flow and heat transfer in helically coiled pipes. Part 3:  
Assessment of turbulence models, parametrical study and proposed  
correlations for fully turbulent flow in the case of zero pitch**

*F. Castiglia, P. Chiovaro, M. Ciofalo, M. Di Liberto, P.A. Di Maio, I. Di Piazza, M.  
Giardina, F. Mascari, G. Morana, G. Vella*



MODELLING FLOW AND HEAT TRANSFER IN HELICALLY COILED PIPES. PART 3: ASSESSMENT OF TURBULENCE MODELS, PARAMETRICAL STUDY AND PROPOSED CORRELATIONS FOR FULLY TURBULENT FLOW IN THE CASE OF ZERO PITCH

F. Castiglia, P. Chi ovaro, M. Ci ofalo, M. Di Liberto, P.A. Di Maio, I. Di Piazza, M. Gi ardina, F. Mascari, G. Morana, G. Vella

Settembre 2010

Report Ricerca di Sistema Elettrico

Accordo di Programma Ministero dello Sviluppo Economico – ENEA

Area: Produzione e fonti energetiche

Tema: Nuovo Nucleare da Fissione

Responsabile Tema: Stefano Monti, ENEA



**CIRTEN**  
**CONSORZIO INTERUNIVERSITARIO**  
**PER LA RICERCA TECNOLOGICA NUCLEARE**

**UNIVERSITA' DI PALERMO**  
**DIPARTIMENTO DI INGEGNERIA NUCLEARE**

## **Modelling flow and heat transfer in helically coiled pipes**

**Part 3: Assessment of turbulence models, parametrical study and proposed  
correlations for fully turbulent flow in the case of zero pitch**

## **Modellazione numerica del campo di moto e dello scambio termico in condotti elicoidali**

**Parte 3: Valutazione di modelli di turbolenza, studio parametrico e  
correlazioni proposte per moto turbolento nel caso di passo nullo**

F. Castiglia, P. Chiovaro, M. Ciofalo, M. Di Liberto, P.A. Di Maio,

I. Di Piazza, M. Giardina, F. Mascari, G. Morana, G. Vella

**CIRTEN-UNIPA RL-1206/2010**

**Palermo, Novembre 2009**

*Lavoro svolto in esecuzione delle linee progettuali LP2 punto G dell'AdP ENEA MSE del 21/06/07,  
Tema 5.2.5.8 – “Nuovo Nucleare da Fissione”*

# CONTENTS

<b>ABSTRACT</b>	<b>3</b>
<b>NOMENCLATURE</b>	<b>4</b>
Greek symbols	4
Subscripts / superscripts	5
<b>1. INTRODUCTION: FLOW AND HEAT TRANSFER IN CURVED PIPES AND COILS</b>	<b>6</b>
<b>2. MODELS AND METHODS</b>	<b>10</b>
2.1. Numerical methods	10
2.2. Turbulence modelling	11
2.3. Grid independence assessment	11
2.4. Validation by comparison with DNS results	12
2.5. Validation by comparison with experimental pressure drop results	14
2.6. Validation by comparison with experimental heat transfer results	15
<b>3. PARAMETRICAL STUDY</b>	<b>16</b>
3.1. The data set	16
3.2. The power-law dependence: a discussion	18
3.3. Heat - momentum transfer analogy	19
<b>4. CONCLUSIONS</b>	<b>20</b>
<b>REFERENCES</b>	<b>22</b>
<b>TABLES</b>	<b>25</b>
<b>FIGURES</b>	<b>29</b>

## ABSTRACT

The present report follows a companion one (F. Castiglia *et al.*, Modelling flow and heat transfer in helically coiled pipes - Part 2: Direct numerical simulations for laminar, transitional and weakly turbulent flow in the case of zero pitch, Rapporto CIRTEN-UNIPA RL-1205/2010), in which DNS results were presented for toroidal pipes (i.e., helically coiled pipes with zero pitch or torsion) assuming two values of the curvature ( $\delta=0.1$  and  $0.3$ ) and a range of Reynolds numbers such that laminar steady, laminar unsteady (transitional) and chaotic, or weakly turbulent, flow was obtained. In that previous report, a particular emphasis was placed on the periodic and quasi-periodic flow regimes obtained for intermediate values of the Reynolds number, which had been poorly or not at all documented in the literature.

Here, computational results are presented for fully turbulent flow and heat transfer in toroidal pipes of different curvature. Based on the existing literature, the results, although still obtained for the case of zero pitch, can be regarded with excellent approximation as representative of helically coiled heat exchangers, as will be better discussed in Section 1 and in the Conclusions.

Following a grid refinement study, grid independent predictions from alternative turbulence models ( $k-\varepsilon$ , SST  $k-\omega$  and RSM- $\omega$ ) are compared with DNS results from the previous study and with experimental pressure drop and heat transfer data. Using the SST  $k-\omega$  and RSM- $\omega$  models, pressure drop results in excellent agreement with literature data and the Ito correlation are obtained. For heat transfer, the literature is not comparably complete or accurate, but a satisfactory agreement is obtained in the range of available data. Unsatisfactory results, both for pressure drop and heat transfer, are given by the  $k-\varepsilon$  model with wall functions.

Following the validation study, the RSM- $\omega$  model is applied to the computation of friction coefficients and Nusselt numbers in the range  $Re = 1.4 \cdot 10^4 \sim 8 \cdot 10^4$ ,  $Pr = 0.7 \sim 5.6$  and  $\delta$  (pipe curvature) =  $3 \cdot 10^{-3} \sim 0.3$ . Power-law correlations are proved to be unsuitable to fit the Re-, Pr- and  $\delta$ -dependence of the Nusselt number, while the use of a properly formulated momentum-heat transfer analogy collapses all results with high accuracy.

## NOMENCLATURE

$a$	tube radius [m]
$b$	coil pitch divided by $2\pi$ [m]
$c$	coil radius [m]
$c_p$	specific heat [ $\text{J kg}^{-1} \text{K}^{-1}$ ]
De	Dean number, $\text{Re}\sqrt{\delta}$
$f$	Darcy-Weisbach friction coefficient
$k$	turbulent kinetic energy [ $\text{m}^2 \text{s}^{-2}$ ]
Nu	Nusselt number, $q_w 2a / \chi(T_b - T_w)$
Pr	Prandtl number, $\mu c_p / \chi$
$q_w$	wall heat flux [ $\text{W m}^{-2}$ ]
Re	Reynolds number, $u_{av} 2a / \nu$
$r$	radial coordinate [m]
$T$	temperature [K]
$u$	axial velocity [ $\text{m s}^{-1}$ ]
$u_\tau$	friction velocity [ $\text{m s}^{-1}$ ]
$y^+$	distance from the wall in wall units, $y\nu/u_\tau$

### Greek symbols

$\delta$	dimensionless curvature, $a/c$
$\lambda$	torsion, $b/c$
$\beta$	modified torsion parameter, see Eq. (3)
$\delta_T^+$	thermal sublayer thickness in wall units
$\nu$	kinematic viscosity [ $\text{m}^2 \text{s}^{-1}$ ]
$\rho$	density [ $\text{kg m}^{-3}$ ]
$\chi$	thermal conductivity [ $\text{W m}^{-1} \text{K}^{-1}$ ]
$\theta$	azimuthal angle [ $^\circ$ ]

$\tau_w$  wall shear stress [Pa]  
 $\omega$  turbulence frequency [ $s^{-1}$ ]

### **Subscripts**

*av* average  
*b* bulk  
*cr* critical  
*MIN* minimum  
*MAX* maximum  
*RAD* radial  
*red* reduced  
*s* straight tube  
*SEC* section  
*w* wall  
 $\theta$  azimuthal

### **Superscripts**

*loc* local

# 1. INTRODUCTION: FLOW AND HEAT TRANSFER IN CURVED PIPES AND COILS

Although curved pipes are used in a wide range of applications, flow in curved pipes is relatively less well known than that in straight ducts. The earliest observations on the complexity involved are due to Thomson [1], while Grindley and Gibson [2] noticed the effect of curvature on the fluid flow during experiments on the viscosity of air. Williams *et al.* [3] observed that the location of the maximum axial velocity is shifted towards the outer wall of a curved pipe. Later, Eustice [4] showed the existence of a secondary flow by injecting ink into water.

Due to the imbalance between inertial and centrifugal forces, a secondary motion develops in the cross section of a curved pipe. In his pioniering work, Dean [5] wrote the Navier-Stokes equations in a cylindrical reference frame, and, under the hypothesis of small curvatures and small Reynolds numbers, derived power series solutions for the stream function of the secondary motion and for the axial velocity. From his analysis a new governing parameter emerged, the Dean number  $De = Re \sqrt{\delta}$ , which couples together inertial and centrifugal effects. Dean showed that two symmetric secondary cells develop with a characteristic velocity scale  $u_{av} \sqrt{\delta}$ ,  $u_{av}$  being the average axial velocity and  $\delta$  the dimensionless curvature defined in the following. A thorough literature review of flow in curved pipes has been presented by Berger *et al.* [6].

An important engineering application of curved pipes are helical coils, which are used as heat exchangers and steam generators in power plant because of their higher heat transfer efficiency with respect to straight pipe configurations; for a comparison between conventional and helically coiled heat exchangers see [7]. In particular, helical coils are also used as steam generators in some ‘generation IV’ nuclear reactors like IRIS [8]; this last application motivated the present study.

A schematic representation of a helical pipe with its main geometrical parameters is shown in Fig. 1. A helical coil can be geometrically described by the coil radius  $c$ , the pipe radius  $a$ , and the coil pitch  $2\pi b$ . The inner side will be indicated with  $I$ , the outer side with  $O$ .

The dimensionless curvature and torsion can be defined as:

$$\delta = \frac{a}{c} \quad (1)$$

$$\lambda = \frac{b}{c} \quad (2)$$

Helical coils reduce to curved (toroidal) pipes when  $\lambda = 0$ . Germano [9] presented for the first time an orthogonal reference system for helical pipes. His work prompted a number of asymptotic analyses in the laminar (low-Reynolds number) range, aimed to studying the effect of torsion on the flow. Within this strand, remarkable are the works of Chen and Jan [10], Kao [11], Xie [12], Jinsuo and Benzhao [13]. By their asymptotic approach, these authors all conclude that torsion  $\lambda$  has a second order effect on the flow with respect to the first order effect of curvature  $\delta$ . The effect of curvature is the occurrence of two counter-rotating vortices in the cross section, while the effect of torsion is an azimuthal rotation of the centres of circulation of such cells, with a global loss of symmetry with respect to the equatorial midline I-O. In particular, Jinsuo and Benzhao [13] showed that the mass flow rate and thus the friction coefficient depend on the curvature  $\delta$ , while the contribution of torsion is at most of the fourth order. Yamamoto *et al.* [14] performed an experimental study on pressure drop in helical coils. They introduced a modified torsional parameter  $\beta$  which, in the present notation, can be expressed as

$$\beta = \sqrt{\frac{\delta}{2}} \cdot \frac{\lambda}{\sqrt{1 + \lambda^2}} \quad (3)$$

and let the Reynolds number  $Re$  vary from  $5 \cdot 10^3$  to  $2 \cdot 10^4$ , the curvature  $\delta$  from 0.01 to 0.1 and the parameter  $\beta$  from 0.45 to 1.72. The authors showed that in the laminar range the influence of torsion on the friction coefficient is negligible for  $\beta < 1$ . In the turbulent range, the authors found that the experimental data depend only on curvature for  $\beta < 0.5$ . In any case these values of the torsional parameter  $\beta$  can be attained only for very large curvatures and are far larger than those encountered in practical engineering applications. For example, for the steam generator of the IRIS nuclear reactor [8] the torsional parameter  $\beta$  ranges approximately from 0.01 to 0.025.

The negligible effect of torsion on the global parameters is reflected in the proposed empirical correlations. A review of experimental results for the friction coefficient in helical coils is presented

by Ali [15]; the most popular correlations are those by Ito [16]:

$$f = \frac{64}{\text{Re}} \cdot \frac{21.5 \cdot \text{De}}{(1.56 + \log_{10} \text{De})^{5.73}} \quad (\text{laminar flow}) \quad (4)$$

$$f = 0.304 \cdot \text{Re}^{-0.25} + 0.029\sqrt{\delta} \quad (\text{turbulent flow}) \quad (5)$$

Here and in the following  $f$  is the Darcy-Weisbach friction coefficient and the Reynolds number is defined on the basis of the tube diameter as:

$$\text{Re} = \frac{u_{av} 2a}{\nu} \quad (6)$$

where  $\nu$  is the kinematic viscosity of the fluid.

Coherently with the theoretical considerations in [13] and with the experimental evidence in [14], no practical influence of torsion is revealed by Eqs. (4) and (5), i.e. the friction coefficient depends only on the curvature  $\delta$  and on the Reynolds number  $\text{Re}$  in most of the applications.

As regards the transition to turbulence, Srinivasan *et al.* [17] studied it on the basis of friction coefficient measurements, observing that the effect of curvature is to delay transition with respect to straight pipes. Although the reasons for this have not yet been fully explained by turbulence theory [6], the authors propose the following correlation for the critical Reynolds number in curved tubes:

$$\text{Re}_{cr} = 2.1 \cdot 10^3 (1 + 12\sqrt{\delta}) \quad (7)$$

This correlation presents the correct asymptotic behaviour for straight ducts ( $\delta=0$ ) and predicts  $\text{Re}_{cr} \approx 4.6 \cdot 10^3$  for  $\delta=0.01$  and  $\text{Re}_{cr} \approx 10^4$  for  $\delta=0.1$ , values considerably higher than that ( $\text{Re}_{cr} \approx 2.1 \cdot 10^3$ ) valid for straight pipes.

Cioncolini and Santini [18] performed an experimental investigation of the friction coefficient in helical coils in a wide range of curvatures ( $\delta=2.7 \cdot 10^{-3}$ -0.14) with low values of the torsion parameter ( $\beta=10^{-4}$ - $2 \cdot 10^{-2}$ ), which ensures negligible torsional effects, and Reynolds numbers ranging from  $10^3$  to  $7 \cdot 10^4$ . The authors found a good agreement with Ito's correlations both in the laminar and in the turbulent range. As it happens for other relatively complex geometries [19], the lack of an abrupt transition from laminar to turbulent flow is evidenced by a smooth and monotonic behaviour of the friction coefficient with  $\text{Re}$  for high values of the curvature  $\delta$ .

Reviews of heat transfer and friction coefficient correlations in helical or curved ducts are presented by Naphon and Wongwises [20] and by Vashist *et al.* [21]; unfortunately, these reviews do not always specify the experimental conditions and, in some cases, do not make a clear distinction between tube-side and shell-side heat transfer correlations. Here and in the following the classical definition of the Nusselt number for the inner (tube) side will be used:

$$Nu = \frac{q_w 2a}{\chi (T_b - T_w)} \quad (8)$$

where  $q_w$  is the average wall heat flux,  $\chi$  is the fluid thermal conductivity,  $T_b$  is the bulk fluid temperature and  $T_w$  is the wall temperature.

Rogers and Mayhew [22] propose the following power-law correlation based on experimental data:

$$Nu = 0.023 Re^{0.85} Pr^{0.4} \delta^{0.1} \quad (9)$$

which can be viewed as a curved-duct modification for of the well-known Dittus-Bölder correlation. It should be noticed that Eq. (9) does not exhibit the correct asymptotic behaviour for small  $\delta$ , predicting  $Nu=0$  for straight pipes. Many other experimental studies have been performed in the 1960s and the 1970s on the average heat transfer rate in curved and helical pipes ([23], [24]); only some of these investigations explored the influence of the Prandtl number on heat transfer, and very few investigated the local heat transfer rate distribution.

More recently, Xin and Ebadian [25] presented an experimental study on heat transfer in helical pipes; the authors explored two values of curvature, i.e.  $\delta=0.027$  and  $0.08$ ,  $Re$  ranging from  $5 \cdot 10^3$  to  $1.1 \cdot 10^5$ , and used three different fluids, i.e. air ( $Pr=0.7$ ), water ( $Pr=5$ ), and ethylene glycol ( $Pr=175$ ), thus covering a broad range of Prandtl numbers. The authors found that results for air and water ( $0.7 < Pr < 5$ ) can be approximated by the following correlation:

$$Nu = 0.00619 Re^{0.92} Pr^{0.4} (1 + 3.455\delta) \quad (10)$$

with an RMS deviation of 18%. Eq. (10) has the advantage of a reasonable asymptotic behaviour for straight pipes. However, a Reynolds exponent larger than 0.8 does not seem realistic, if one considers that this last value is limited to straight pipes while in more complex geometries, involving separation and reattachment, an exponent *less* than 0.8 is usually found [26].

## 2. MODELS AND METHODS

### 2.1 Numerical methods

The general purpose code ANSYS CFX 11 was used for all the numerical simulations presented in this paper. The code employs a coupled technique, which simultaneously solves all the transport equations in the whole domain through a false time-step algorithm. The linearized system of equations is preconditioned in order to reduce all the eigenvalues to the same order of magnitude. The multi-grid approach reduces the low frequency error, converting it to a high frequency error at the finest grid level; this results in a great acceleration of convergence. Although, with this method, a single iteration is slower than a single iteration in the classical decoupled (segregated) SIMPLE approach, the number of iterations necessary for a full convergence to a steady state is generally of the order of  $10^2$ , against typical values of  $10^3$  for decoupled algorithms.

The computational domain was a small portion of a curved tube of circular cross section; as discussed in the previous section, torsion was not considered in the present study because, for geometries of practical relevance, it has been shown that torsion does not significantly affect the global parameters  $f$  and  $Nu$ .

To simulate fully developed flow and heat transfer, periodic boundary conditions were imposed at inlet-outlet, and no-slip condition for the velocity at the wall; a constant source term was added to the RHS of the axial momentum equation as the driving force per unit volume which balances pressure drop per unit length. Only one half of the section was modelled, and symmetry boundary conditions were used along the Inner-Outer symmetry plane, as shown in Fig. 2.

As thermal boundary condition, a constant wall temperature  $T_w$  was imposed. In order to apply periodic inlet-outlet boundary conditions also for the temperature field, a local energy source term was applied to compensate the wall heat flux. Taking account of the definition of the Nusselt number based on the bulk temperature  $T_b$ , this local source term must be proportional to the local axial velocity. With this treatment, the bulk temperature and the Nusselt number tend to stable values once convergence is reached. The Nusselt number thus obtained represents the asymptotic value of  $Nu$  for fully developed flow.

## 2.2 Turbulence modelling

Different turbulence models were used in the numerical simulations presented in this work.

The classic  $k$ - $\varepsilon$  model [27] was adopted with a near-wall treatment (the “scalable” option in CFX-11) which practically ignores the solution within the viscous sublayer  $y^+ < 11$ , and imposes the universal (wall law) logarithmic solution in the first point outside of it; this approach is basically equivalent to the classic wall-function treatment with the first near-wall point outside of the viscous sublayer.

The SST (Shear Stress Transport)  $k$ - $\omega$  model by Menter [28] is formulated to solve the viscous sublayer explicitly, and requires several computational grid points inside this latter. The model applies the  $k$ - $\omega$  model close to the wall, and the  $k$ - $\varepsilon$  model (in a  $k$ - $\omega$  formulation) in the core region, with a blending function in between. It was originally designed to provide accurate predictions of flow separation under adverse pressure gradients, but has since been applied to a large variety of turbulent flows and is now the default and most commonly used model in CFX-11 and other CFD codes.

The second order Reynolds stress- $\omega$  model (RSM- $\omega$ ) was extensively used within this work. In this model, the  $\omega$ -based formulation allows for an accurate near wall treatment like in SST  $k$ - $\omega$ ; diffusion terms in the Reynolds stress transport equations are treated by a simple eddy diffusivity approach, whereas great care is placed in the modelling of redistribution terms (pressure-strain rate correlations). For the exact formulation of the model and the values of the various constants, see [29].

## 2.3 Grid independence assessment

A careful grid independence study was carried out in order to provide internally coherent numerical results. The five meshes used in this study are summarized in Table 1 and are indicated as meshes 1 through 5 from the coarsest to the finest. The meshes are of the multi-block structured type, and are identified by the parameters  $N_{RAD}$  and  $N_{\theta}$  as shown in Fig. 2.  $N_{SEC}$  represents the total number of cells in the cross section;  $\Delta r_{MAX}/\Delta r_{MIN}$  is the ratio of maximum/minimum cell size in the radial direction (outer block), while the last column  $y^+_{min}$  in Table 1 is the location (in wall units  $v/u_{\tau}$ ) of the point closest to the wall for the highest Reynolds number considered,  $Re=8 \cdot 10^4$ .

Meshes 1 and 2 do not differ in the number of nodes, but only in the wall stretching parameter

$\Delta r_{MAX}/\Delta r_{MIN}$  (and therefore in the wall resolution); the same holds for meshes 3 and 4. Meshes 2 and 3 have different number of nodes, but the same wall resolution. Meshes 3, 4 and 5 ensure respectively 8, 27 and 63 points within the hydrodynamic viscous sublayer  $y^+ < 11$  for  $Re=8 \cdot 10^4$ .

For all values of the Prandtl number simulated, up to  $Pr=5.6$ , a correct resolution of the thermal conductive sublayer must also be ensured in order to guarantee grid-independence of the thermal results and physically consistent solutions. Experimental data reported in [30] provide a value of the thickness of the thermal viscous sublayer  $\delta_T^+ = 7.55$  (in wall units) for  $Pr=5.9$ ; on the basis of this estimate, meshes 3, 4 and 5 include 6, 22 and 51 points, respectively, within the thermal sublayer in the most critical case ( $Pr=5.6$ ,  $Re=8 \cdot 10^4$ ).

The results of the grid-independence study are reported in Table 2 for a typical value of the curvature,  $\delta=0.1$ , and the RSM- $\omega$  model. An asymptotic tendency of the global values to converge with mesh refinement, from mesh 1 to mesh 5, can be observed. There is a significant variation from mesh 1 to mesh 2 due to the increased resolution of the viscous sublayer, and from mesh 2 to 3 due to the increased number of nodes. Both the Darcy-Weisbach friction coefficient and the Nusselt number converge, showing differences of less than 0.5% between mesh 4 and mesh 5.

On the basis of these results, mesh 4 was adopted for all the subsequent simulations conducted in the present study. Note that mesh 5 would require CPU time three times higher.

## 2.4 Validation by comparison with DNS results

In this section, computational results obtained by using the different turbulence models are compared with the results of a fully resolved direct numerical simulation (DNS). This was performed by using a grid of about  $4 \cdot 10^6$  nodes with  $y^+ \approx 1.2$  at the first grid point close to the wall; statistics were computed over about 20 characteristic times  $a/u_\tau$  (LETOTs).

The case studied is characterized by a curvature  $\delta=0.3$ , a Reynolds number  $Re=1.4 \cdot 10^4$ , and a Prandtl number  $Pr=0.86$ . The values of the parameters  $Re$  and  $\delta$  are the most critical for turbulence model validation, because, as it will be discussed in the next section, the largest discrepancies from experimental data are obtained for the highest curvature and the lowest Reynolds number.

Fig. 3 shows a comparison of the DNS average flow field in the cross section with results from the

turbulence models ( $k-\varepsilon$  with near-wall treatment, SST  $k-\omega$ , RSM- $\omega$ ). The dimensionless temperature  $(T-T_w)/(T_b-T_w)$ , the dimensionless velocity  $u/u_{av}$ , and the dimensionless turbulent kinetic energy  $k/u_{av}^2$  are represented respectively in the first, second and third column of the figure. In the DNS results, the Dean circulation is evidenced by the shape of the contours, which are deformed by the secondary jet along the wall; the Dean vortex close to the inner region is most clearly evidenced by the  $k$  contours. SST  $k-\omega$  and RSM- $\omega$  yield similar velocity and temperature fields which are very close to that predicted by DNS, while the  $k-\varepsilon$  model with wall functions captures these structures only roughly. The main axial velocity contour field shows slightly better results for RSM with respect to SST in capturing flow features close to the Dean vortex.

Fig. 4 shows profiles of the dimensionless temperature as a function of the dimensionless radial coordinate  $r/a$  along the Inner-Outer direction, with  $r/a=-1$  at the inner side and  $r/a=1$  at the outer side. This figure shows the different ability of the models to reproduce the main (horizontal) thermal stratification. As it was expected,  $k-\varepsilon$  completely fails in describing this stratification, while both SST and RSM results are in good agreement with DNS, with a more accurate prediction from RSM in all regions; in particular, the maximum temperature is predicted better by RSM with respect to SST.

Fig. 5 shows the local wall shear stress  $\tau_w^{loc}$ , normalized by the mean wall shear stress  $\tau_w$ , as a function of the azimuthal angle  $\theta$  which increases from 0 at the inner side (I) to 180° at the outer side (O). For SST and RSM, the agreement is good for low angles ( $\theta < 45^\circ$ ), where both models remarkably capture the Dean vortex features and the detachment point location. In the central and outer regions both models exhibit a lesser accuracy, predicting a uniform distribution of  $\tau_w$  for  $\theta > 90^\circ$ , whereas DNS predicts a slight monotonic increase with a maximum for  $\theta = 180^\circ$ . The  $k-\varepsilon$  predictions are of far lower quality.

Fig. 6 shows the local Nusselt number  $Nu^{loc}$ , normalized by the mean Nusselt number  $Nu$ , as a function of the azimuthal angle  $\theta$ . A correct overall behaviour of the plotted quantity is obtained using the SST and RSM turbulence models, which predict a growing heat transfer rate going from the inner to the outer region, although an underestimate of  $Nu^{loc}$  by about 10% can be observed at the outer side ( $\theta = 180^\circ$ ). For low angles ( $\theta < 45^\circ$ ), the SST and RSM models capture the Dean vortex features and the

detachment location. As in the  $\tau_w$  plot,  $k$ - $\varepsilon$  predictions are far less satisfactory and exhibit a more uniform behaviour of  $Nu^{bc}$ .

## 2.5 Validation by comparison with experimental pressure drop results

A comparison of results from different turbulence models with the experimental data obtained by Cioncolini and Santini [18] is discussed in this section. Turbulence models were used well into the laminar range in order to test their intrinsic ability to predict laminarization and to provide solutions in the transition region.

Fig. 7 shows a comparison of experimental and computational results for the Darcy-Weisbach friction coefficient versus  $Re$  for the geometry “COIL09” of [18], characterized by a curvature  $\delta=9.64 \cdot 10^{-3}$ . The experimental data are in excellent agreement with Ito’s correlations. At this relatively low value of the curvature, in the transitional region the data exhibit a “memory” of the transitional “knee” typical of the straight pipe, with a friction coefficient approximately constant from  $Re=4 \cdot 10^3$  to  $Re=10^4$ .

The  $k$ - $\varepsilon$  model with the above mentioned near-wall treatment is totally inadequate to simulate the correct behaviour of  $f$ , yielding a heavy underprediction of this quantity even in the fully turbulent region. The SST and RSM results are both in good agreement with the experimental data in the turbulent range, and are able to predict laminarization at low  $Re$ . However, they give less satisfactory results in the transitional region, predicting a smooth connection between laminar and turbulent curves; thus, they can not be fully recommended for transitional flows.

Fig. 8 shows the same comparison for a higher value of curvature, i.e. “COIL01” of [18], characterized by  $\delta=0.143$ . In this case the experimental data suggest, like in complex geometries [19], a smooth transition between the laminar and the turbulent region, without any “knee”; the experimental friction coefficient curve is even smoother than in the previous case of Fig. 7 because of the more intense secondary circulation induced by the higher curvature. Also in this case the experimental data are reproduced with high accuracy by the Ito correlation, which therefore, although proposed half a century ago, can be regarded as an excellent one in its range of validity. The  $k$ - $\varepsilon$  model underpredicts  $f$  in the whole Reynolds number range, while SST and RSM yield a good agreement

with the experimental data in the turbulent range and behave better than in the lower-curvature case in Fig 7 also in the laminar and transitional regions.

## 2.6 Validation by comparison with experimental heat transfer results

For heat transfer, a comparison was made with the experimental results of Xin and Ebadian [25]. Unfortunately, these authors investigate only two values of curvature,  $\delta=0.027$  and  $0.08$ , and present most of their results in a reduced form that does not allow the original data to be retrieved. Fig. 9 shows a comparison between computational and experimental results for Nu for  $\delta=0.08$ , a Prandtl number of 5 (cold water in the experiments), and Reynolds numbers in the range  $10^4 \sim 5 \cdot 10^4$ . Due to the experimental method used, an additional (not declared) uncertainty of the order of  $\pm 1$  is intrinsically present in the Prandtl number of the experimental study for water; therefore, it is safer to state that in the experiments Pr is in the range  $4 \sim 6$ , i.e.  $5 \pm 1$ . Both SST and RSM explicitly resolve the wall thermal and mechanical sublayers, with the first computational point at  $y^+ < 0.25$  in all cases, and a substantial grid-independence of the results. In the turbulent range, both SST and RSM slightly overestimate the Nusselt number, which could partly be due to the above mentioned uncertainties on Pr. The correlation provided by Rogers and Mayhew, Eq.(9), falls in between the numerical results and the experimental data.

Fig. 10 shows a comparison of the reduced Nusselt number  $Nu_{red} = Nu Pr^{-0.4} (1 + 3.455\delta)^{-1}$  as a function of the Reynolds number. Circles indicate the experimental data for two test sections with curvatures  $\delta=0.027$  and  $0.08$  and  $Pr=0.7 \sim 5$ ; error bars indicate the declared uncertainty on the data. Triangles show numerical results obtained using the RSM- $\omega$  turbulence model in the same range of curvature and Pr. Computational results fall within the scatter band of the experimental data; however, the experimental data themselves exhibit a relatively large dispersion once reduced by the proposed law of Eq.(10).

From the above discussions, it emerges that the SST and RSM models ensure a satisfactory and comparable accuracy in heat transfer predictions. In this work, the higher order RSM model was eventually chosen to perform the extensive parametrical study documented in the following section.

### 3. PARAMETRICAL STUDY

#### 3.1 The data set

A parametrical computational study on flow and heat transfer in curved ducts was carried out by using the second order Reynolds Stress Model (RSM- $\omega$ ), in which the boundary layer was explicitly resolved and the mesh resolution guaranteed  $y^+ < 0.25$  at the first grid point close to the wall even in the most critical condition. The Reynolds number  $Re$  was made to vary in the range  $1.4 \cdot 10^4 \sim 8 \cdot 10^4$ , the Prandtl number  $Pr$  in the range  $0.7 \sim 5.6$  and the curvature  $\delta$  in the range  $0 \sim 0.3$ . The range chosen for the Reynolds number ensures that all cases simulated fall in the full turbulent region even for the highest values of curvature and the lowest value of the Reynolds number. The range chosen for the Prandtl number covers air ( $Pr=0.7$ ) and water ( $Pr=1$  for water close to the saturation temperature,  $Pr=5.6$  for ambient temperature water), while the range chosen for the curvature  $\delta$  includes straight pipes ( $\delta=0$ ) and highly curved ducts ( $\delta=0.3$ ), with several curvatures of practical interest in between.

A full-matrix dataset was produced including six values of  $Re$  ( $1.4 \cdot 10^4$ ,  $2 \cdot 10^4$ ,  $2.8 \cdot 10^4$ ,  $4 \cdot 10^4$ ,  $5.6 \cdot 10^4$ ,  $8 \cdot 10^4$ ), seven values of  $Pr$  ( $0.7$ ,  $1$ ,  $1.4$ ,  $2$ ,  $2.8$ ,  $4$ ,  $5.6$ ), and six values of the curvature  $\delta$  ( $0$ ,  $3 \cdot 10^{-3}$ ,  $10^{-2}$ ,  $3 \cdot 10^{-2}$ ,  $0.1$ ,  $0.3$ ), for a total of 252 test cases. The results from all the test cases, i.e. the computed values of the Darcy friction coefficient  $f$  and of the mean Nusselt number  $Nu$ , are summarized in Table 4. Fig. 11 shows  $f$  against  $Re$  for the different  $\delta$  in a doubly logarithmic scale; the friction coefficient exhibits the classic monotonic decreasing behaviour with  $Re$ , while the influence of  $\delta$  is to progressively increase  $f$ . Fig. 12 shows a parity plot between computed values of the Darcy friction coefficient and those predicted by the Ito correlation (5) for turbulent flow for all the test cases in Table 4, with the exception of those at  $\delta=0.3$  which lie outside of the range of validity of Eq. (5). An excellent agreement can be observed, with an rms dispersion of a few %; the largest discrepancies are obtained for the largest  $f$ , corresponding to the lowest Reynolds number and the largest values of the curvature. Fig. 13 shows  $Nu$  against  $Re$  for the different  $\delta$  in a doubly logarithmic scale and for two values of  $Pr$ , i.e.  $Pr=0.7$  and  $5.6$ . The Reynolds number dependence of  $Nu$  follows (at least approximately) a power law, but its slope varies with  $Pr$  and  $\delta$ .

### 3.2 The power-law dependence: a discussion

Indicating with  $f_s$  and  $Nu_s$  respectively the friction coefficient and the Nusselt number for straight ducts, and with  $f$  and  $Nu$  the corresponding quantities for a curved geometry, the ratios  $f/f_s$  and  $Nu/Nu_s$  will be used as reference quantities for discussion in this section.

If a power-law like that proposed by Xin and Ebadian, Eq.(10), held for the Nusselt number in curved ducts, and the Dittus-Bölder correlation  $Nu_s=0.023\cdot Re^{0.8}Pr^{0.4}$  in straight ducts, the ratio  $Nu/Nu_s$  should behave as:

$$\frac{Nu}{Nu_s} = c \cdot Re^m Pr^n \cdot (1 + d \cdot \delta) \quad (11)$$

with  $d=3.455$ ,  $m=0.12$ ,  $n=0$ ,  $c=0.269$ .

Otherwise, if the Rogers correlation, Eq.(9), held for curved ducts, one would obtain:

$$\frac{Nu}{Nu_s} = c \cdot Re^m Pr^n \cdot \delta^p \quad (12)$$

with  $c=1$ ,  $m=0.05$ ,  $n=0$ ,  $p=0.1$ .

Apart from the exact values of the various constants, Eqs.(11) and (12) predict that power laws for the Re- and Pr-dependence, and a linear or power-law for the  $\delta$ -dependence, should be observed in the computational results. However, this turns out *not* to be the case.

In particular, Fig. 14 shows a log-log diagram of  $f/f_s$  and  $Nu/Nu_s$  as functions of  $\delta$ , for a fixed Reynolds number of  $2 \cdot 10^4$  and all the values of the Prandtl number studied; Fig. 15 shows the same quantities in a linear-linear scale. The hydrodynamic solution, and thus the ratio  $f/f_s$ , do not depend on the Prandtl number, and Figs. 14-15 show that the friction coefficient ratio in a curved duct grows with the curvature  $\delta$ . The Nusselt ratio  $Nu/Nu_s$  grows with the curvature regardless of the Prandtl number, but increases more rapidly for the lower values of Pr. The two graphs reveal that neither a linear nor a power-law dependence upon the curvature  $\delta$  can be found in the results for  $f/f_s$  or  $Nu/Nu_s$ . The function  $(1+d\cdot\delta)$  of Eq. (11), proposed in [25], can perhaps be applied to a small range of curvatures, but it appears as a linearization of a more complex dependence; the power-law  $\delta^p$  dependence of Eq. (12) is also not respected and, moreover, does not provide the correct asymptotic

behaviour of  $Nu/Nu_s$  for  $\delta \rightarrow 0$ .

Figure 15 shows a log-log diagram of  $f/f_s$  and  $Nu/Nu_s$  as functions of  $Pr$ , for a fixed Reynolds number of  $2 \cdot 10^4$  and different values of the curvature. The hydrodynamic solution and thus the ratio  $f/f_s$  do not depend on the Prandtl number, and therefore the corresponding curves are horizontal lines for any value of  $\delta$ . In the range examined, the Nusselt number ratio remains always smaller than the friction coefficient ratio. An inverse power-law dependence on  $Pr$  can be observed for the Nusselt ratio at all values of  $\delta$ , but the power exponent increases in absolute value with the curvature instead of being a constant: therefore, the dependence of  $Nu/Nu_s$  upon  $Pr$  predicted by Eqs. (11) and (12) is not confirmed, while a  $Pr^{-n\delta}$  law would be more coherent with the results. A similar behaviour is observed for higher Reynolds numbers. For a given value of the curvature, the slope of the  $Nu/Nu_s$  lines decreases in absolute value with the Reynolds number, as shown in Fig. 17 where  $Nu/Nu_s$  is plotted against  $Pr$  for various  $Re$ . A hypothetical power law dependence on  $Pr$  should be of the form  $Pr^{-n\delta g(Re)}$ ,  $g(Re)$  being a decreasing positive function of the Reynolds number.

Figure 18 shows a log-log diagram of  $f/f_s$  and  $Nu/Nu_s$  as functions of  $Re$ , for  $Pr=1$  and  $4$  and different values of the curvature  $\delta$ . The Reynolds number dependence appears to be weak, especially at moderate values of the curvature  $\delta$ , i.e.  $\delta \leq 0.03$ . Therefore, also in this case a hypothetical Reynolds number exponent for  $Nu/Nu_s$  should be negative, which is consistent with the above mentioned fact that in complex flows with recirculation the  $Nu-Re$  power law exponent is systematically lower than the value  $0.8$  typical of simple geometries. Moreover, such exponent would depend on  $\delta$  and  $Pr$ , and only a  $Re^{-m\delta g(Pr)}$  law would be approximately consistent with the numerical results.

The above analysis shows that the simple, empirically based, power law dependences proposed in the literature can not account for the complexity of the real functional dependences, and a different approach is necessary for a correct regression of the data set.

### 3.3 Heat - momentum transfer analogy

Churchill [31] presents a critical review of the classical algebraic analogies between heat, mass and momentum transfer, and derives an exact integral formulation of the momentum-heat transfer analogy for circular ducts. The author shows that, surprisingly, very popular power-law formulas like the

Colburn analogy:

$$\text{Nu} = \text{Pr}^{1/3} \text{Re} \cdot (f/8) \quad (13)$$

are not physically founded or theoretically based, but are only used for traditional reasons or because they are easy to manipulate. For example, Churchill shows that the correct asymptotic behaviour of the Nusselt number for  $\text{Pr} \rightarrow \infty$  should be  $\text{Re}(f/8)^{1/2}$ , and not  $\text{Re}(f/8)$  as prescribed by the Reynolds-Colburn analogy.

Pethukov [32] correlated experimental values of the Nusselt number for turbulent straight pipe flow and for  $0.5 \leq \text{Pr} \leq 2000$  by the expression:

$$\text{Nu} = \frac{\text{Pr Re}(f/8)}{1.07 + 12.7 \sqrt{f/8} \cdot (\text{Pr}^{2/3} - 1)} \quad (14)$$

Eq. (14) is based on the same general integral analogy used later by Churchill [31], with an eddy diffusivity model for the Reynolds stresses, and therefore it rests on a more sound theoretical ground than the simple Dittus-Bölder power-law. In fact, for straight pipes Eq. (14) provides a greater accuracy, with a deviation of only a few percent with respect to experimental data.

Therefore, it is worth checking whether Pethukov's analogy, Eq. (14), can successfully be applied also to curved pipes, i.e. can lead to a reduction of the dispersion with respect to power-law correlations. In the literature on curved ducts, only Seban and McLaughlin [23] introduce the friction coefficient as a modelling parameter for the Nusselt number, but maintain a power-law dependence on the Prandtl number.

In Fig. 19, a parity plot is presented of the CFD-computed Nusselt number against the Pethukov predictive formula (14), in which for the Darcy friction coefficient the values computed by CFD for curved geometries, Table 4, were used. The numerical data collapse very well with an RMS dispersion of only 1-2%. As Fig. 12 suggests, very similar results would be obtained by correlating computed values of Nu with those predicted by substituting the values of  $f$  given by Ito's correlation (5) into the Pethukov analogy (14). Fig. 20 shows such a parity plot of Nu against the Pethukov formula (14). This shows that the combination of Eqs. (5) and (14) predicts Nu in curved ducts with the same accuracy of the present RSM- $\omega$  simulations and is far superior to previously suggested correlations.

## 4. CONCLUSIONS

The comparison of alternative turbulence models showed that the SST  $k$ - $\omega$  eddy viscosity / eddy diffusivity model and the second order Reynolds Stress- $\omega$  model give comparable results for the friction coefficient  $f$  and the Nusselt number  $Nu$ , the latter being slightly better in predicting details of velocity and temperature profiles when compared with direct numerical simulations. Moreover, both models are able to predict laminarization and thus are applicable with only a moderate error also to Reynolds numbers below the transition to fully turbulent flow (i.e, in the laminar and transitional range). The standard  $k$ - $\varepsilon$  model, with a near-wall treatment equivalent to using classic wall functions, yields a severe underprediction of both  $f$  and  $Nu$ .

The application of the RSM- $\omega$  model in the fully turbulent regime ( $Re > 1.4 \cdot 10^4$ ) for different values of the curvature  $\delta$  yields pressure drop results in excellent agreement with experimental data [18] and with the correlation proposed by Ito [16]. Heat transfer results obtained for different Prandtl numbers in the range 0.7~5.6 are in good agreement with published experimental results [25] but are poorly described by simple power-law correlations. Instead, the use of a properly formulated momentum-heat transfer analogy, notably in the form known as the Pethukov correlation [32], yields an excellent reduction of all heat transfer data, using either the CFD-computed friction coefficient or that predicted by the Ito correlation [16].

As in all companion reports on the same subject, it is worth noting that, although the main interest is in finite-pitch helical coils of the kind used in heat exchangers, and particularly in the steam generators for the IRIS reactor, results obtained for zero pitch (toroidal) pipes are of great relevance and help a better understanding of the role of Reynolds number and curvature to be obtained without the extra complexity introduced by an additional parameter (torsion). Of course, this is possible because a large bulk of experimental and computational results presented in the last decades have shown that, within certain limits, coil torsion, which differentiates a helical pipe from a toroidal one, has only a higher order effect on flow features, so that a moderate torsion does not significantly affect global quantities such as the friction factor and the Nusselt number, nor the critical Reynolds numbers for flow regime transitions. For example, in their experimental investigations for turbulent flow and

curvatures  $\delta$  ranging from 0.026 and 0.088, Xin and Ebadian [25] did not observe any influence of the coil pitch up to torsions  $\lambda$  of 0.8. Yamamoto *et al.* [14] conducted friction factor measurements for high values of the curvature ( $\delta > 0.5$ ) and showed that this quantity was negligibly affected by torsion provided that a suitably defined torsional parameter  $\beta = (\delta/2)^{1/2} * \lambda / (1 + \lambda^2)^{1/2}$  did not exceed 0.5, a condition corresponding to highly stretched pipes. Their study suggests that, for lower curvatures, the influence of torsion on the friction coefficient would be negligible *at all pitches*. Our own preliminary computations based on RANS turbulence models have shown that, for curvatures typical of the IRIS steam generators ( $\delta \approx 0.02$ ), increasing torsion  $\lambda$  from 0 to 0.3 (a value also typical of the IRIS SG's) led to a decrease of the friction coefficient  $f$  and of the mean Nusselt number  $Nu$  of only ~2%, while a further increase of  $\lambda$  to the very large value of 1 led to a decrease in  $f$  and  $Nu$  of ~6-7% with respect to a toroidal pipe.

## REFERENCES

- [1] Thomson, J., Experimental and numerical study of quenching complex-shaped metallic alloys with multiple, overlapping sprays, Proc. R. Soc. London Ser. A 25 (1876) 5-8.
- [2] Grindley, J.H., Gibson, A.H., On the frictional resistance to the flow of air through a pipe, Proc. R. Soc. London Ser. A 80 (1908) 114-139.
- [3] Williams, G.S., Hubbell, C.W., Fenkell, G.H., On the effect of curvature upon the flow of water in pipes, Trans. ASCE 47 (1902) 1-196.
- [4] Eustice, J., Experiment of streamline motion in curved pipes, Proc. R. Soc. London Ser 85 (1911) 119-131.
- [5] Dean, W.R., Note on the motion of the fluid in a curved pipe, Phil Mag 4 (1927) 208-223.
- [6] Berger, S.A., Talbot, L., Yao, L.S., Flow in curved pipes, Ann Rev Fluid Mech 15 (1983) 461-512.
- [7] Prabhanjan, G.S.V., Raghavan, G. and Rennie, T.J., Comparison of heat transfer rates between a straight tube heat exchanger and a helically coiled heat exchanger, Int Comm Heat mass Transfer 29 (2002) 185-191.
- [8] Carelli, M.D., Conway, L.E., Oriani, L., Petrović, B., Lombardi, C.V., Ricotti, M.E., Barroso, A.C.O., Collado, J.M., Cinotti, L., Todreas, N.E., Grgić, D., Moraes, M.M., Boroughs, R.D., Ninokata, H., Ingersoll, D.T. and Oriolo, F., The design and safety features of the IRIS reactor, Nuclear Eng Design 230 (2004) 151-167.
- [9] Germano, M., On the effect of torsion in a helical pipe flow, J Fluid Mech 125 (1982) 1-8.
- [10] Chen, W.H. and Jan, R., The characteristics of laminar flow in helical circular pipe, J Fluid Mech 244 (1992) 241-256.
- [11] Kao, H.C., Torsion effect on fully developed flow in a helical pipe, J Fluid Mech 184 (1987) 335-356.
- [12] Xie, G.D., Torsion effect on secondary flow in helical pipes, Int J Heat Fluid Flow 11 (1990) 114-119.

- [13] Jinsuo, Z., Benzao, Z., Fluid flow in a helical pipe, *ActaMechanica Sinica* 15 (1999) 299-312.
- [14] Yamamoto, K., Akita, T., Ikeuki, H. and Kita, Y., Experimental study of the flow in a helical circular tube, *Fluid Dynamic Research* 16 (1995) 237-249.
- [15] Ali, S., Pressure drop correlations for flow through regular helical coil tubes, *Fluid Dynamic Research* 28 (2001) 295-310.
- [16] Ito, H., Friction factors for turbulent flow in curved pipes, *J Basic Engineering* 81 (1959) 123-134.
- [17] Srinivasan, S., Nadapurkar, S. and Holland, F.A., Friction factors for coils, *Trans Inst Chem Eng* 48 (1970) T156-T161.
- [18] Cioncolini, A., Santini, L., An experimental investigation regarding the laminar to turbulent flow transition in helically coiled pipes, *Exp Thermal Fluid Science* 30 (2006) 367-380.
- [19] Stasiek, J.A., Collins, M.W., Ciofalo, M. and Chew, P.E., Investigation of flow and heat transfer in corrugated passages – I. Experimental Results, *Int J Heat Mass Transfer* 39 (1996) 149-164.
- [20] Naphon, P., Wongwises, S., A review of flow and heat transfer characteristics in curved tubes, *Renewable and Sustainable Energy Reviews* 10 (2006) 463-490.
- [21] Vashisth, S., Kumar, V., Nigam, D.P.K., A review on the potential application of curved geometries in process industry, *Ind Eng Chem Res* 47 (2008) 3291-3337, 2008.
- [22] Rogers, G.F.C. and Mayhew, Y.R., Heat transfer and pressure loss in helically coiled tubes with turbulent flow, *Int J Heat Mass Transfer* 7 (1964) 1207-1216.
- [23] Seban, R.A. and McLaughlin, E.F., Heat transfer in tube coils with laminar and turbulent flow, *Int J Heat Mass Transfer* 6 (1963) 387.
- [24] Mori, Y. and Nakayama, W., Study of forced convective heat transfer in curved pipes, *Int J Heat Mass Transfer* 11 (1967) 681.
- [25] Xin, R.C. and Ebadian, M.A., The effects of Prandtl numbers on local and average convective heat transfer characteristics in helical pipes, *ASME J Heat Transfer* 119 (1997) 467-473.

- [26] Ciofalo, M. and Collins, M.W.,  $k$ - $\epsilon$  predictions of heat transfer in turbulent recirculating flows using an improved wall treatment, Num Heat Transfer 15 (1989) 21-47.
- [27] Launder, B. E. and Spalding, D. B., The numerical computation of turbulent flows, Computer Methods in Applied Mechanics and Engineering, 3 (1974) 269-289.
- [28] Menter, F. R., Two-equation eddy-viscosity turbulence models for engineering applications, AIAA J 32 (1994) 269-289.
- [29] ANSYS CFX Release 11 User Manual.
- [30] Kays, W.M., Crawford, M.E., Convective heat and mass transfer, McGraw-Hill, New York, 1993.
- [31] Churchill, S.W., Critique of the classical algebraic analogies between heat, mass and momentum transfer, Ind Eng Chem Res 36 (1997) 3866-3878.
- [32] Pethukov, B.S., Heat transfer and friction in turbulent pipe flow with variable physical properties, Adv Heat Transfer 6 (1970) 1-69.

Table 1 – Meshes used for the grid independence study.

<b>MESH</b>	$N_{RAD}$	$N_{\theta}$	$N_{SEC}$	$\Delta r_{MAX}/\Delta r_{MIN}$	$y^+_{min}$
1	38	19	7220	10	3.5
2	38	19	7220	100	0.65
3	130	27	30996	21	0.65
4	130	27	30996	182	0.12
5	250	43	93396	315	0.04

Table 2 – Grid independence results for  $\delta=0.1$ .

<b>MESH</b>	<i>f</i>	Nu(Pr=0.7)	Nu(Pr=5.6)
1	0.025878	206.66	565.04
2	0.026032	207.13	577.96
3	0.026170	207.24	575.85
4	0.026182	211.32	572.84
5	0.026275	211.83	574.60

Table 3 – Comparison with the DNS results for  $\delta=0.3$  and  $Re=1.4 \cdot 10^4$ .

<b>Model</b>	$f$	Nu(Pr=0.86)
$k-\varepsilon$ wall functions	0.033620	48.55
SST $k-\omega$	0.053291	70.28
RSM- $\omega$	0.055601	71.90
DNS	0.048850	65.68

Table 4 – Summary of test cases and results obtained in the present work (mesh 4, RSM- $\omega$ )

$Re \times 10^3$	$\delta \times 10^3$	$f \times 10^2$	Nu						
			Pr=0.7	1	1.4	2	2.8	4	5.6
14	0	3.038	42.06	50.32	59.30	70.08	81.42	94.60	108.09
20	0	2.737	54.61	65.89	78.18	92.97	108.57	126.73	145.32
28	0	2.498	70.18	85.27	101.76	121.68	142.72	167.28	192.43
40	0	2.279	91.90	112.42	134.93	162.20	191.08	224.87	259.53
56	0	2.101	118.92	146.32	176.47	213.13	252.05	297.70	344.59
80	0	1.945	156.77	193.97	235.09	285.22	338.63	401.42	466.03
14	3	3.034	42.07	50.37	59.41	70.26	81.68	94.92	108.46
20	3	2.732	54.65	65.97	78.33	93.21	108.86	127.11	145.74
28	3	2.499	70.24	85.40	101.98	121.98	143.07	167.71	192.89
40	3	2.289	92.04	112.64	135.23	162.58	191.52	225.32	259.96
56	3	2.111	119.15	146.59	176.82	213.54	252.49	298.08	344.85
80	3	1.943	157.00	194.24	235.40	285.54	338.89	401.79	466.27
14	10	3.225	45.02	53.78	63.24	74.48	86.22	99.79	113.57
20	10	2.918	58.40	70.33	83.23	98.64	114.78	133.47	152.50
28	10	2.665	74.98	90.91	108.21	128.95	150.72	175.99	201.76
40	10	2.432	98.14	119.77	143.35	171.74	201.64	236.43	271.95
56	10	2.247	126.99	155.81	187.38	225.53	265.80	312.80	360.85
80	10	2.076	167.52	206.59	249.62	301.80	357.09	421.77	488.02
14	30	3.625	49.86	59.18	69.10	80.82	92.94	106.87	120.98
20	30	3.256	64.34	77.01	90.60	106.70	123.42	142.70	162.24
28	30	2.964	82.29	99.23	117.44	139.16	161.80	187.96	214.51
40	30	2.703	107.35	130.34	155.26	185.02	216.19	252.29	289.01
56	30	2.491	138.50	169.19	202.59	242.69	284.78	333.68	383.49
80	30	2.292	182.08	223.76	269.33	324.21	382.14	449.57	518.42
14	100	4.355	59.69	69.95	80.57	92.84	105.40	119.73	134.21
20	100	3.865	76.00	89.87	104.41	121.36	138.78	158.72	178.88
28	100	3.486	96.20	114.68	134.21	157.15	180.84	208.02	235.53
40	100	3.148	124.34	149.38	175.91	207.64	240.37	278.04	316.22
56	100	2.881	159.25	192.63	228.46	271.02	315.37	366.55	418.50
80	100	2.638	208.01	253.31	302.22	360.62	421.72	492.49	564.47
14	300	5.487	73.13	80.05	91.22	103.76	116.35	130.61	145.00
20	300	4.762	91.15	106.80	122.77	141.00	159.42	180.33	201.40
28	300	4.233	113.43	134.05	155.34	179.87	204.87	233.30	261.95
40	300	3.769	144.49	172.18	201.14	234.81	269.37	308.84	348.63
56	300	3.411	182.96	219.69	258.44	303.85	350.70	404.43	458.74
80	300	3.063	236.54	286.08	338.92	401.37	466.12	540.68	616.25

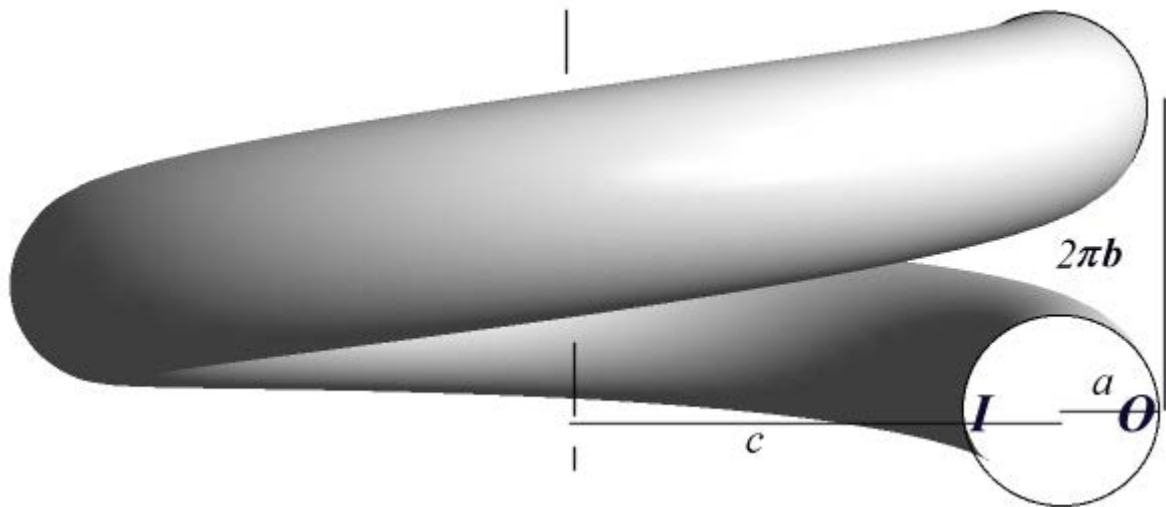


Fig. 1 Schematic representation of a helical pipe with its main geometrical parameters:  $a$ , tube radius;  $c$ , coil radius;  $2\pi b$ , coil pitch. The inner (I) and outer (O) sides of the curved duct are also indicated.

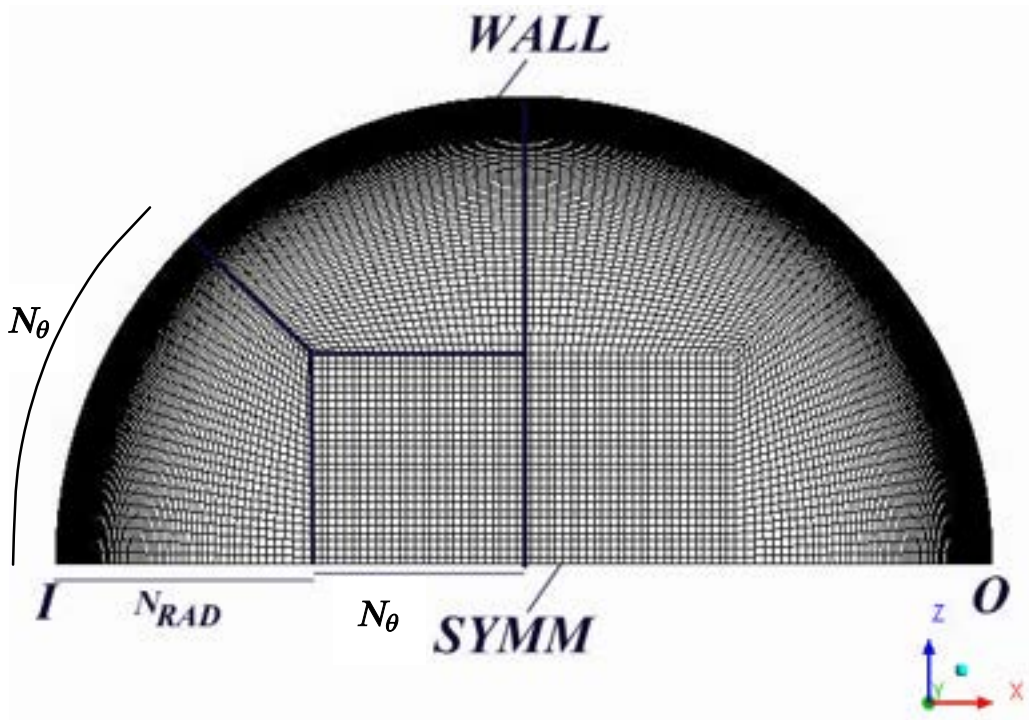


Fig. 2 Mesh (number 4) used to perform the computations. The grid is of the multi-block structured type. The total number of cells in the whole cross section would be  $N_{SEC}=4 \cdot N_\theta (N_\theta + 2 N_{RAD})$ , but only one half of the section is simulated.

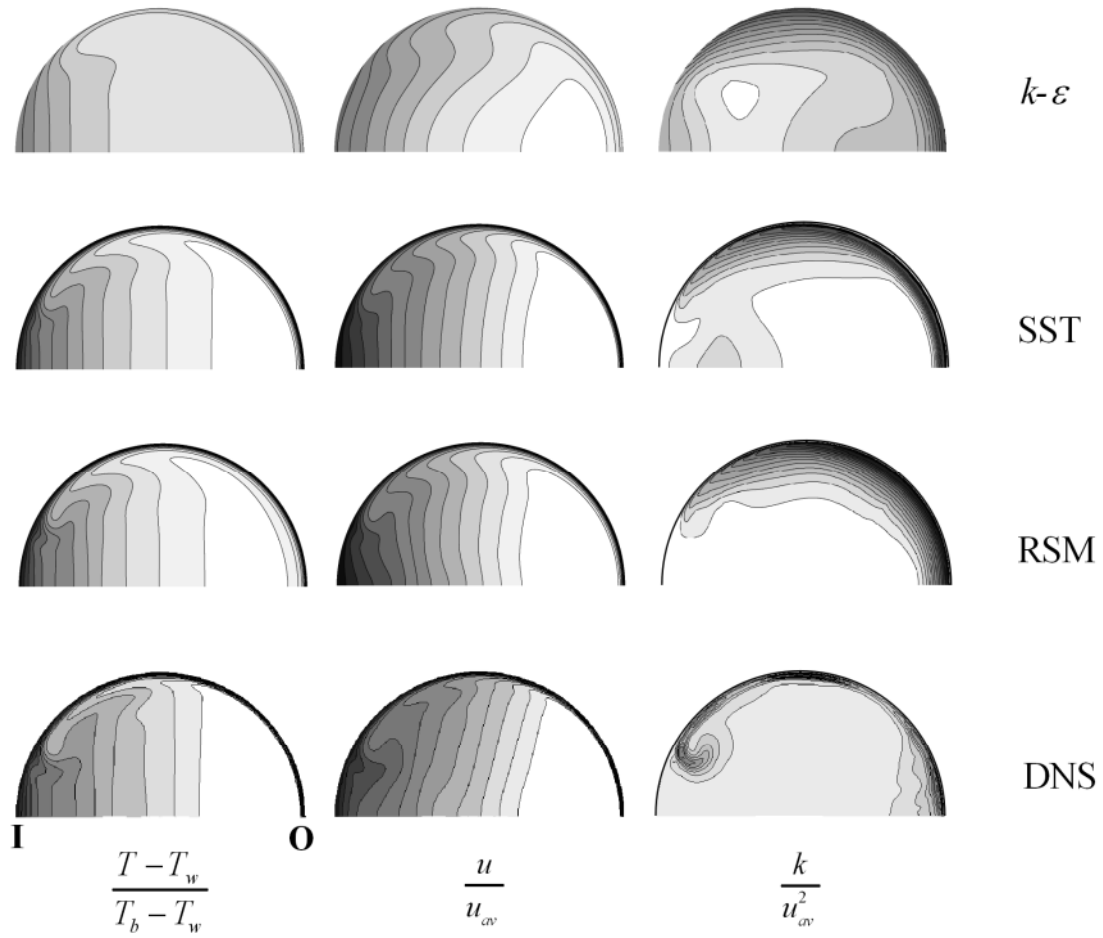


Fig. 3 Comparison of turbulence models and DNS results for  $Re=1.4 \cdot 10^4$ ,  $\delta=0.3$ . The three columns report contours of the dimensionless velocity  $u/u_{av}$  (min=0, max=1.2, interval=0.1), the dimensionless temperature  $(T-T_w)/(T_b-T_w)$  (min=0, max=1.2, interval=0.1), and the dimensionless turbulent kinetic energy  $k/u_{av}^2$  (min=0, max=0.015, interval=0.001).

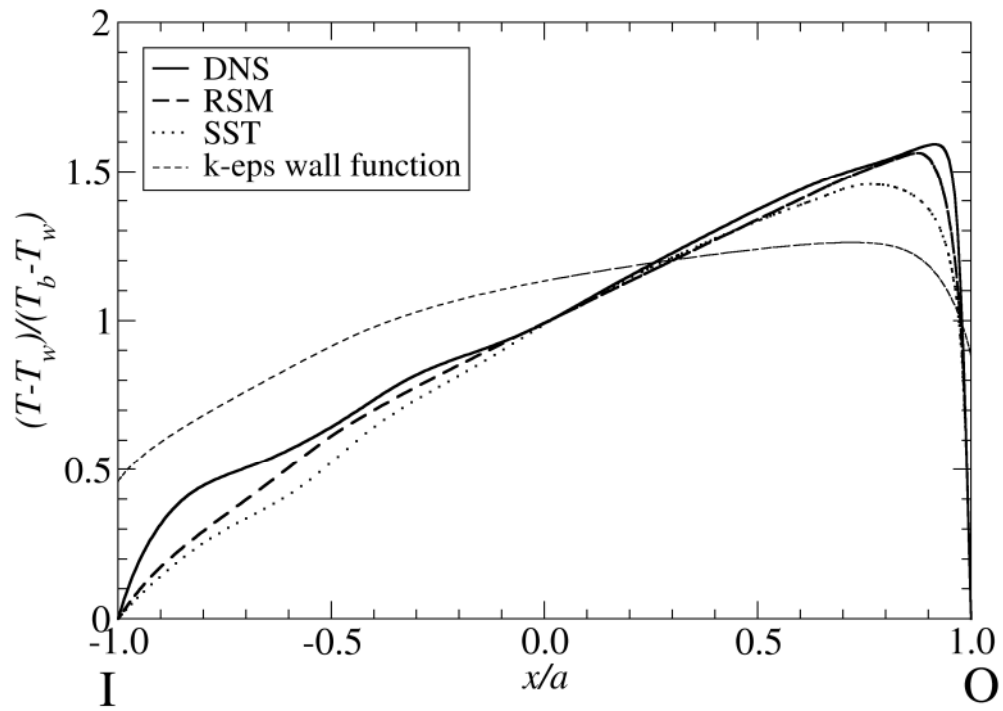


Fig. 4 Profiles of the dimensionless temperature  $(T-T_w)/(T_b-T_w)$  along the Inner-Outer line for  $Re=1.4 \cdot 10^4$ ,  $\delta=0.3$ . Predictions from different turbulence models are compared with DNS average results.

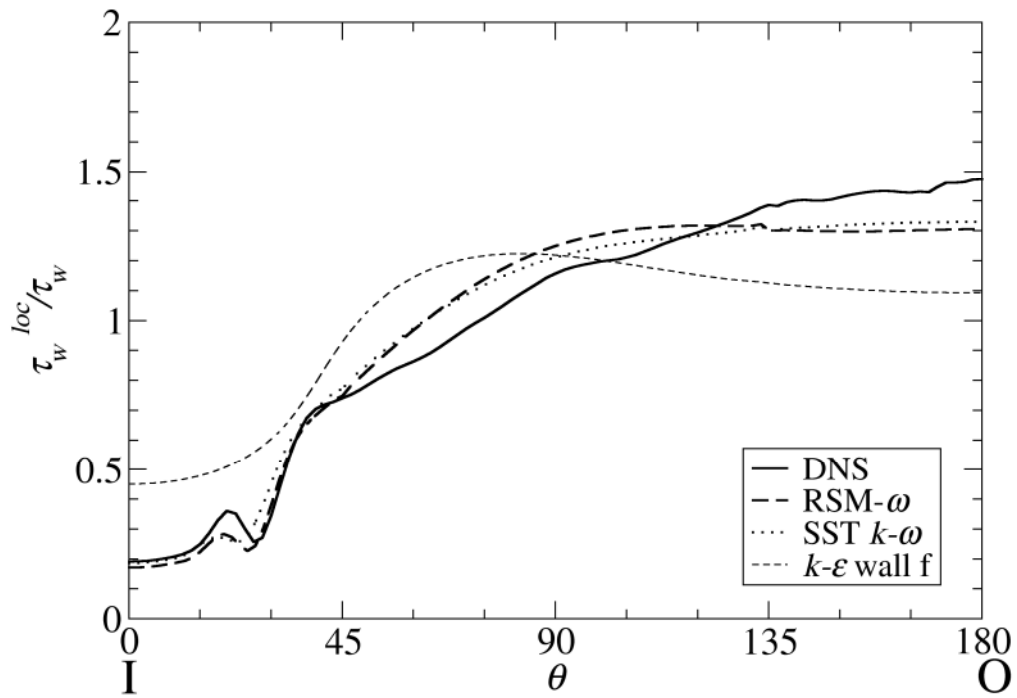


Fig. 5 Profiles of the dimensionless wall shear stress  $\tau_w^{loc} / \tau_w$  along the wall for  $\text{Re}=1.4 \cdot 10^4$  and  $\delta=0.3$ . Predictions from different turbulence models are compared with DNS average results (solid line). The azimuthal angle  $\theta$  runs from 0 at the inner point to  $180^\circ$  at the outer point.

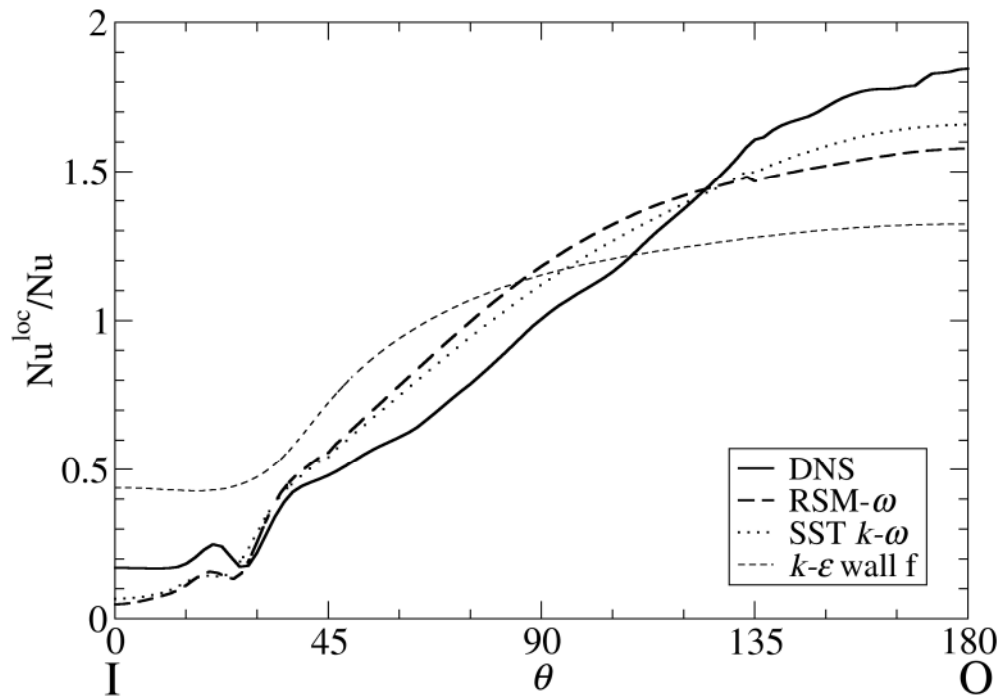


Fig. 6 Profiles of the dimensionless local Nusselt number  $Nu^{loc} / Nu$  along the wall for  $Re=1.4 \cdot 10^4$  and  $\delta=0.3$ . Predictions from different turbulence models are compared with DNS average results (solid line). The azimuthal angle  $\theta$  runs from 0 at the inner point to  $180^\circ$  at the outer point.

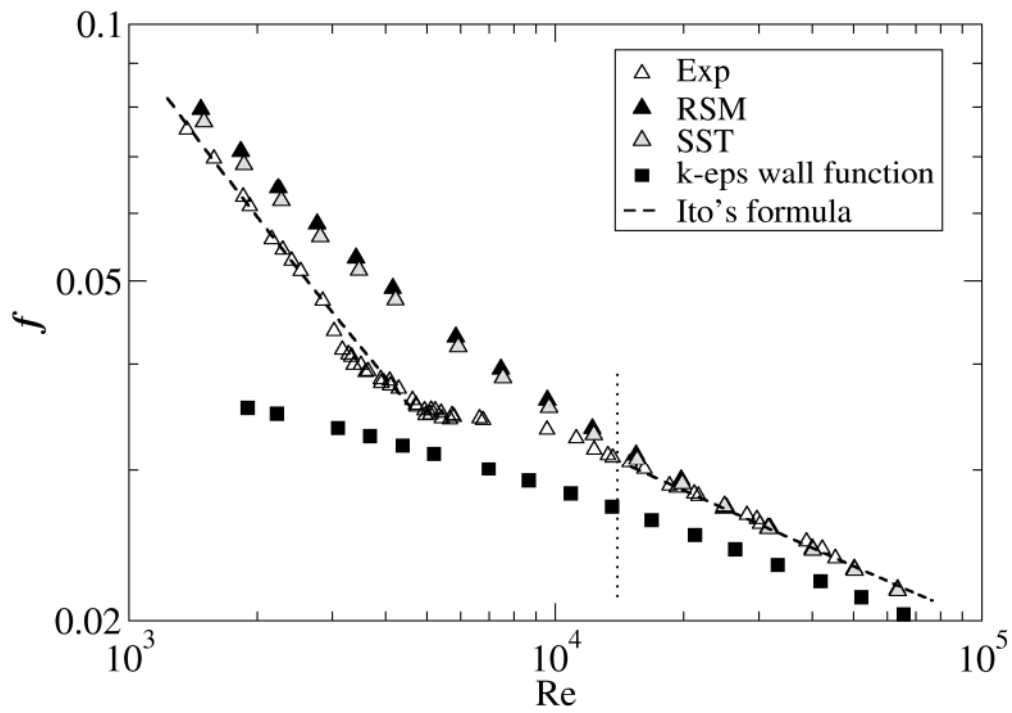


Fig. 7 Darcy-Weisbach friction coefficient as a function of the Reynolds number. Predictions from different turbulence models are compared with experimental data by Cioncolini and Santini for “COIL09” ( $\delta=9.64 \cdot 10^{-3}$ ). Broken lines correspond to the Ito correlations in the laminar and turbulent ranges.

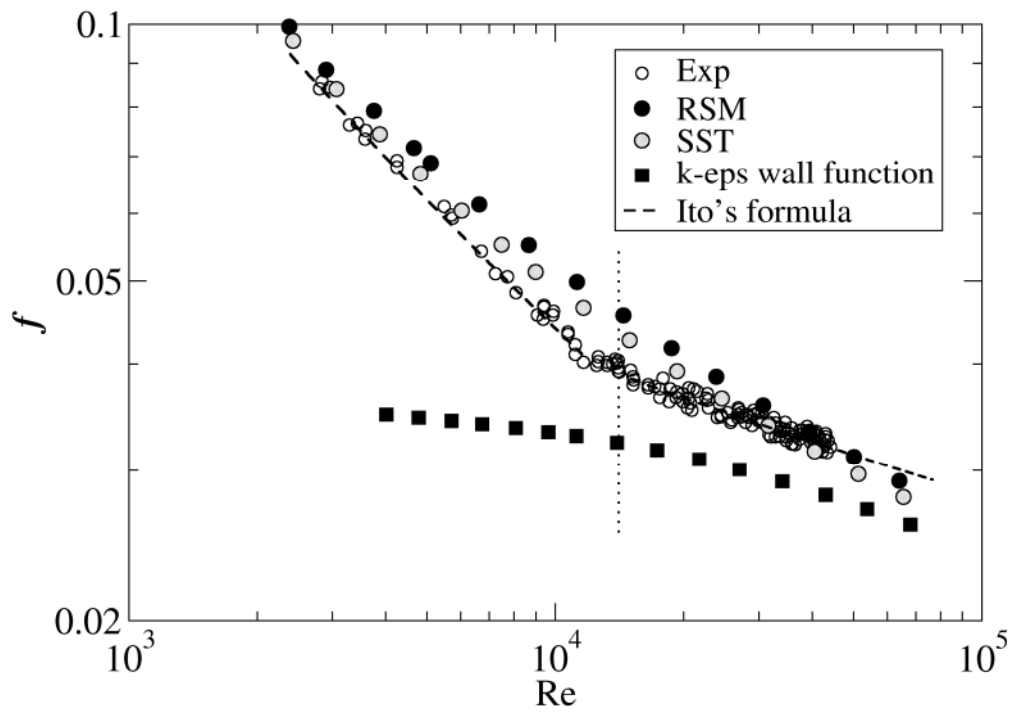


Fig. 8 Darcy-Weisbach friction coefficient as a function of the Reynolds number. Predictions from different turbulence models are compared with experimental data by Cioncolini and Santini for “COIL01” ( $\delta=0.143$ ). Broken lines correspond to the Ito correlations in the laminar and turbulent ranges.

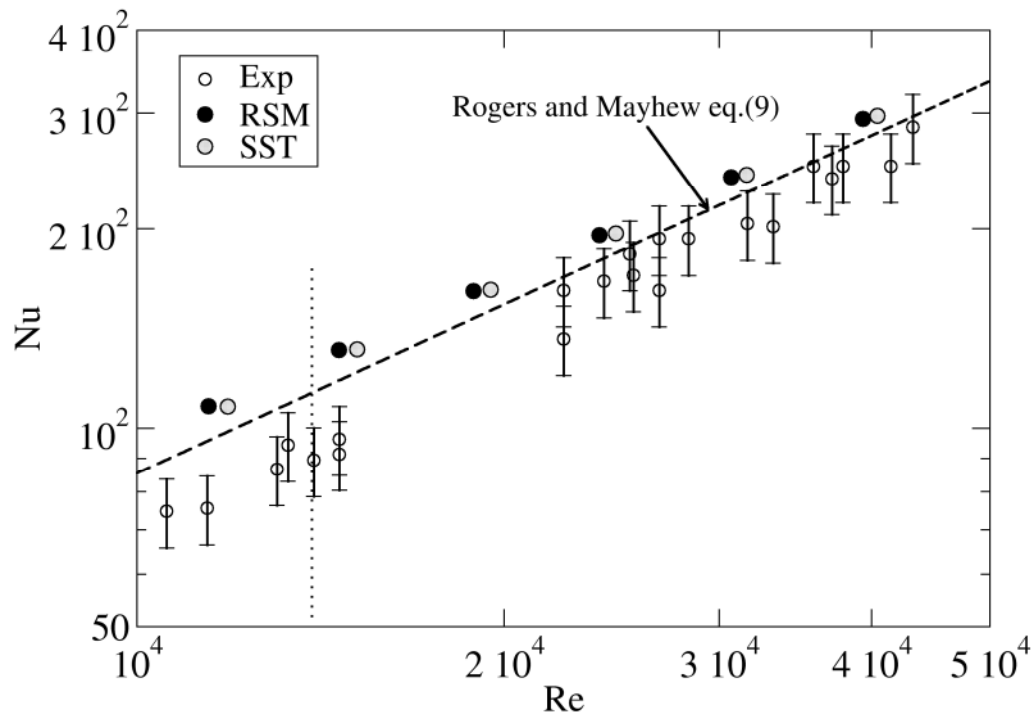


Fig. 9 Comparison of the average Nusselt number obtained by numerical simulations using the SST and RSM models with experimental data by Xin and Ebadian for  $\delta=0.08$ ,  $Pr=5$ . Error bars for the experiments are also shown. The broken line represents the Rogers and Mayhew correlation, Eq. (9).

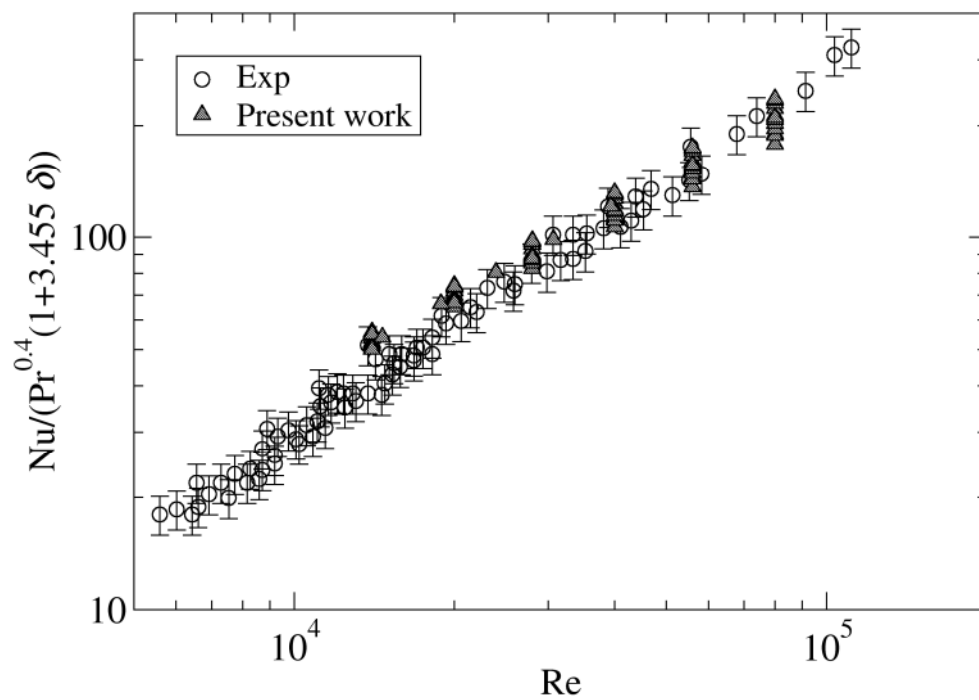


Fig. 10 Comparison of the reduced average Nusselt number  $Nu Pr^{-0.4} (1+3.455 \delta)^{-1}$  obtained by numerical simulations using the RSM model with experimental data by Xin and Ebadian for two values of the curvature ( $\delta=0.027, 0.08$ ) and  $0.7 \leq Pr \leq 5$ .

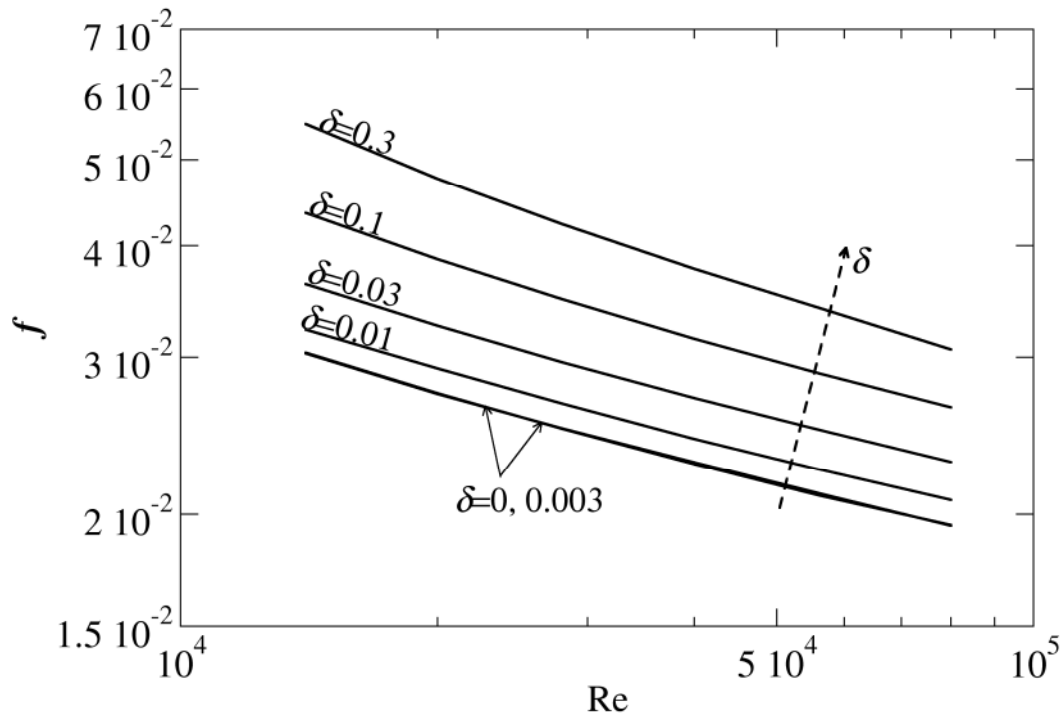


Fig. 11 Darcy-Weisbach friction coefficient as a function of the Reynolds number at different curvatures  $\delta$  for the whole the computational data set. Results for  $\delta=0.003$  and  $\delta=0$  (straight tube) are practically coincident.

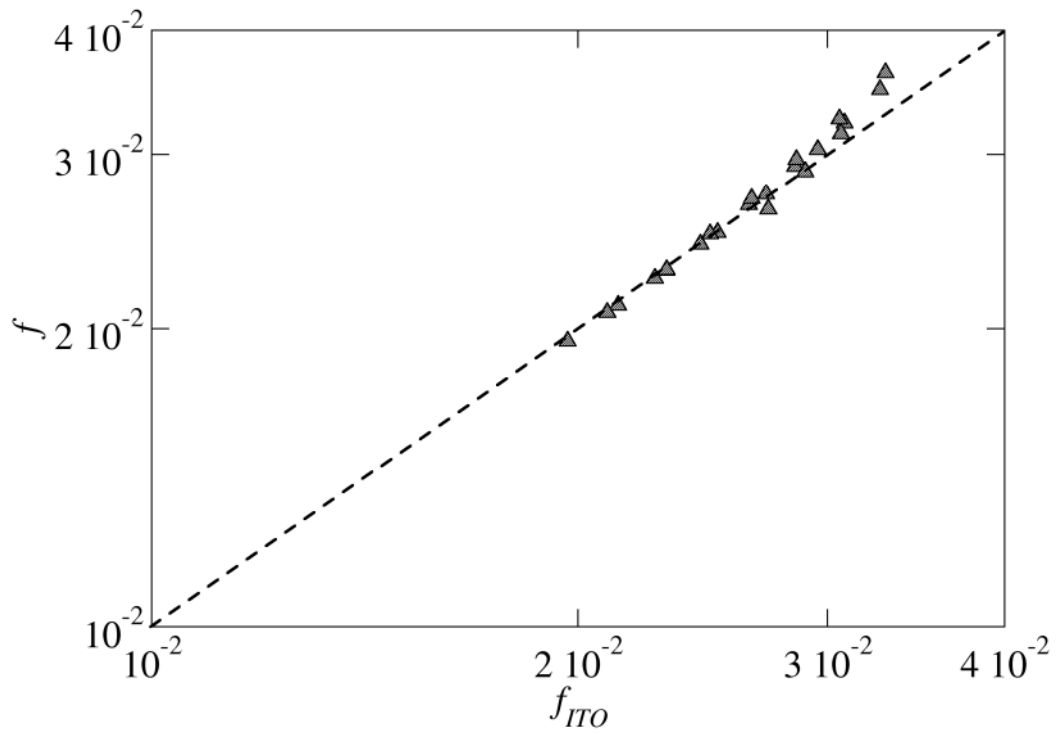


Fig. 12 Parity plot of the RSM computed friction coefficient against that predicted by the Ito correlation.

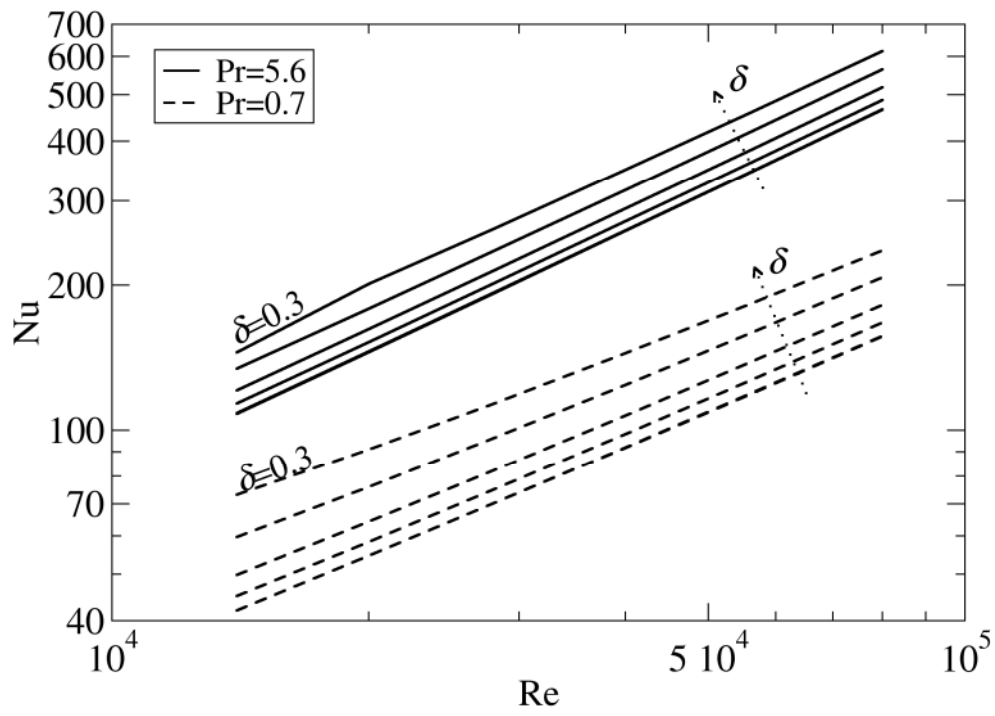


Fig. 13 RSM-computational results for the Nusselt number as a function of the Reynolds number for two values of the Prandtl number,  $Pr=0.7$  and  $5.6$ . Within each family, different curves are characterized by the same values of  $\delta$  as in Fig. 11.

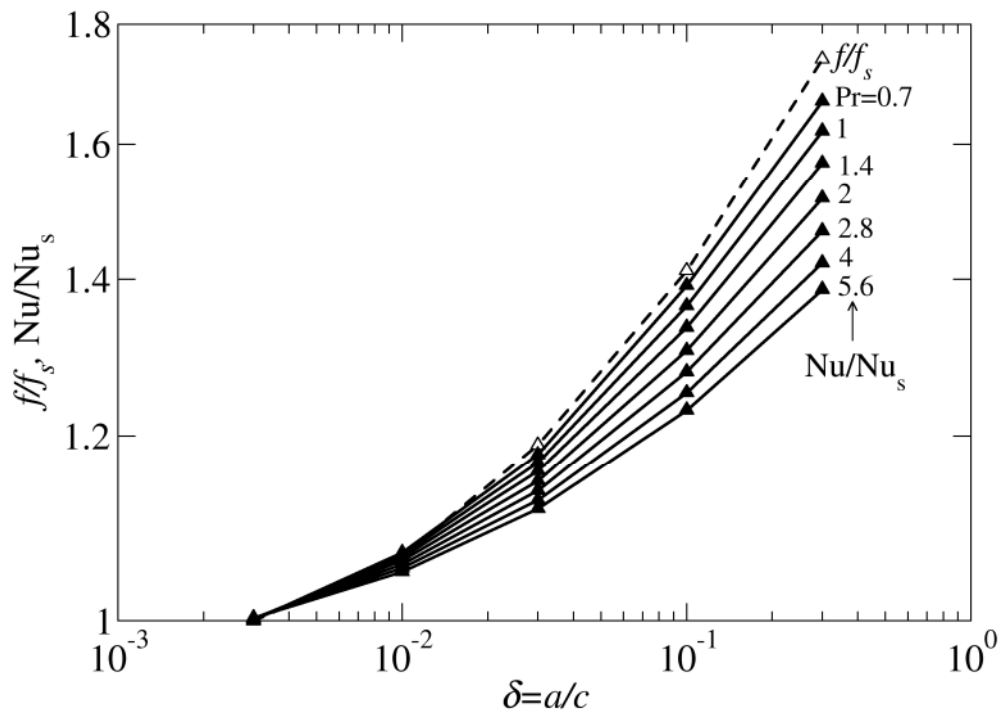


Fig. 14 Doubly logarithmic plot of the RSM-computed relative friction coefficient  $f/f_s$  and Nusselt number  $Nu/Nu_s$  as functions of the curvature  $\delta$  for  $Re=2 \cdot 10^4$  and different values of Pr.

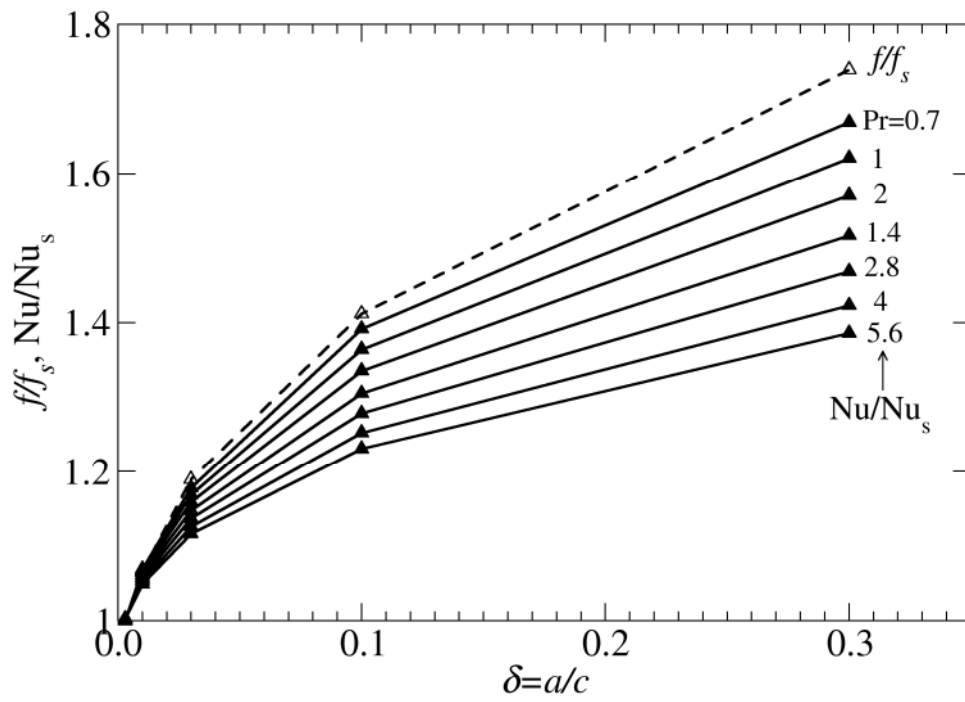


Fig. 15 Doubly linear plot of the RSM-computed relative friction coefficient  $ff_s$  and Nusselt number  $Nu/Nu_s$  as functions of the curvature  $\delta$  for  $Re=2 \cdot 10^4$  and different values of Pr.

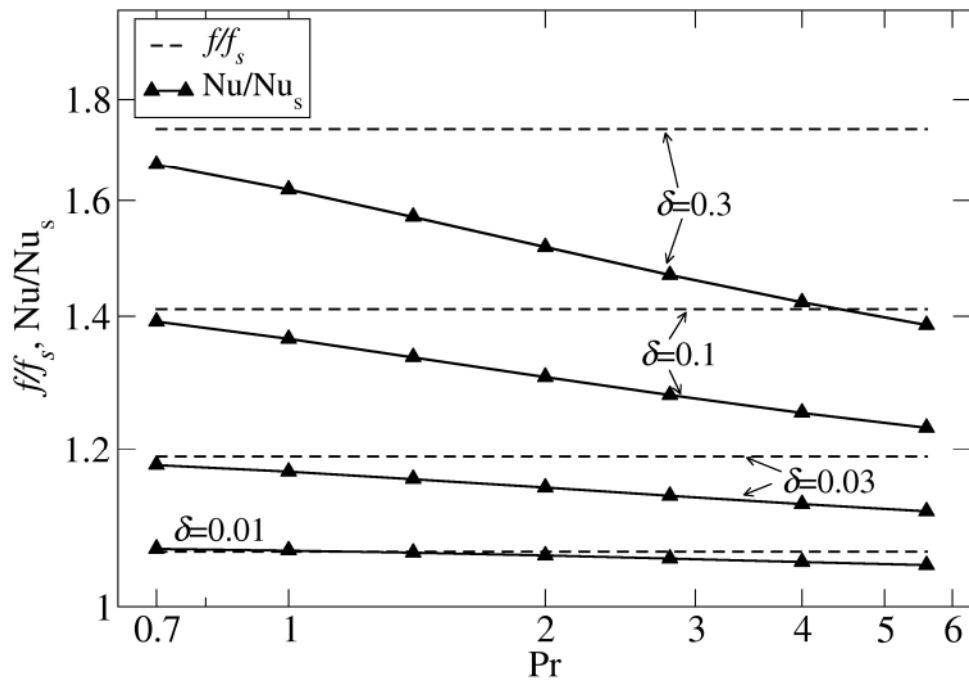


Fig. 16 Doubly logarithmic plot of the RSM-computed relative friction coefficient  $ff_s$  and Nusselt number  $Nu/Nu_s$  as functions of  $Pr$  for  $Re=2 \cdot 10^4$  and different values of  $\delta$ .

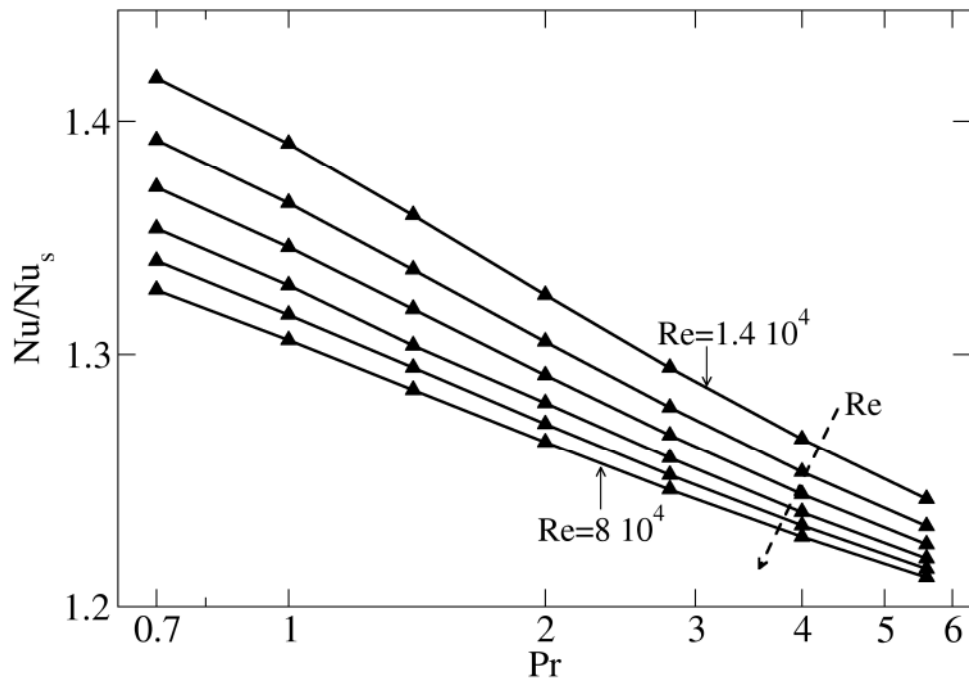


Fig. 17 Doubly logarithmic plot of the RSM-computed relative Nusselt number  $Nu/Nu_s$  as a function of  $Pr$  for  $\delta=0.1$  and  $Re$  ranging from  $1.4 \cdot 10^4$  to  $8 \cdot 10^4$ .

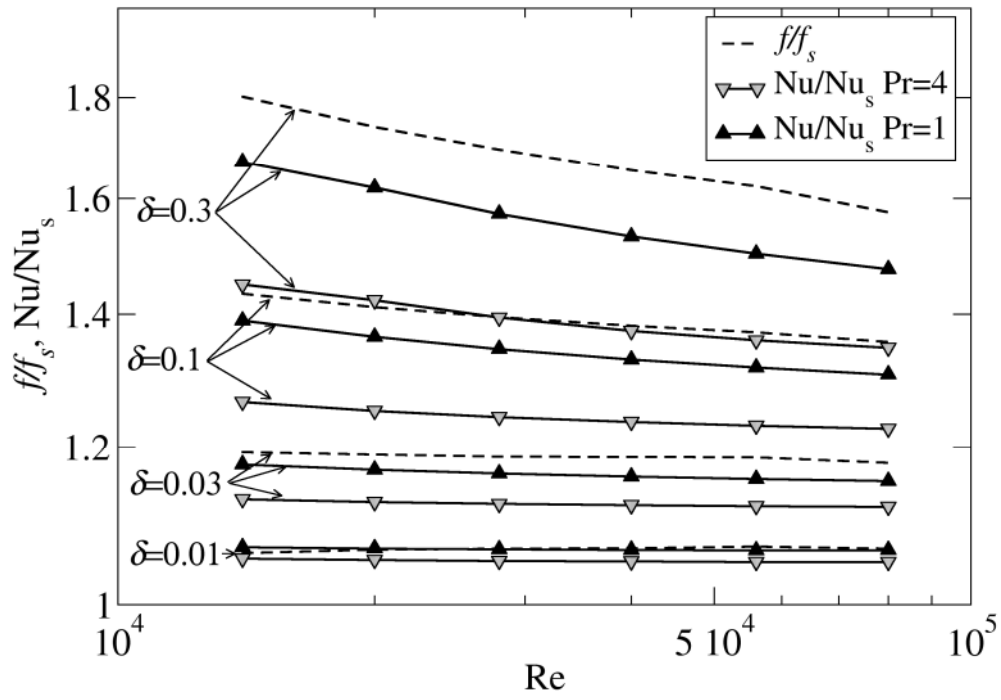


Fig. 18 Doubly logarithmic plot of the RSM-computed relative friction coefficient  $ff_s$  and Nusselt number  $Nu/Nu_s$  as functions of  $Re$  for  $Pr=1$  and  $4$  and different values of  $\delta$ .

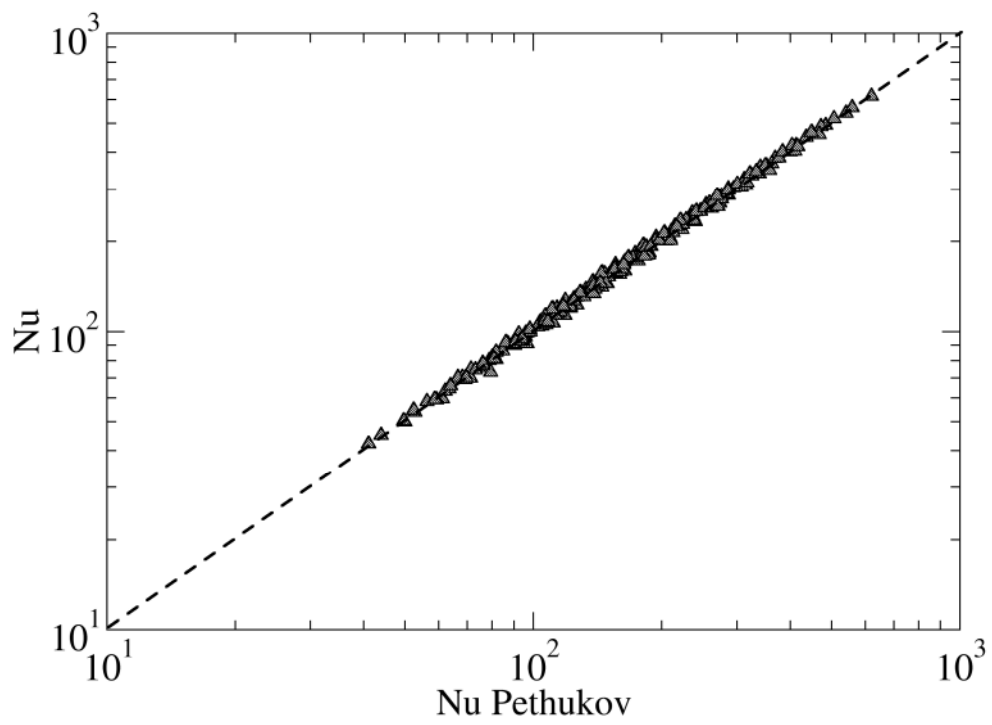


Fig. 19 Parity plot of the mean Nusselt number computed by CFD using the RSM- $\omega$  turbulence model against that predicted by the Pethukov analogy using computed values of  $f$ .

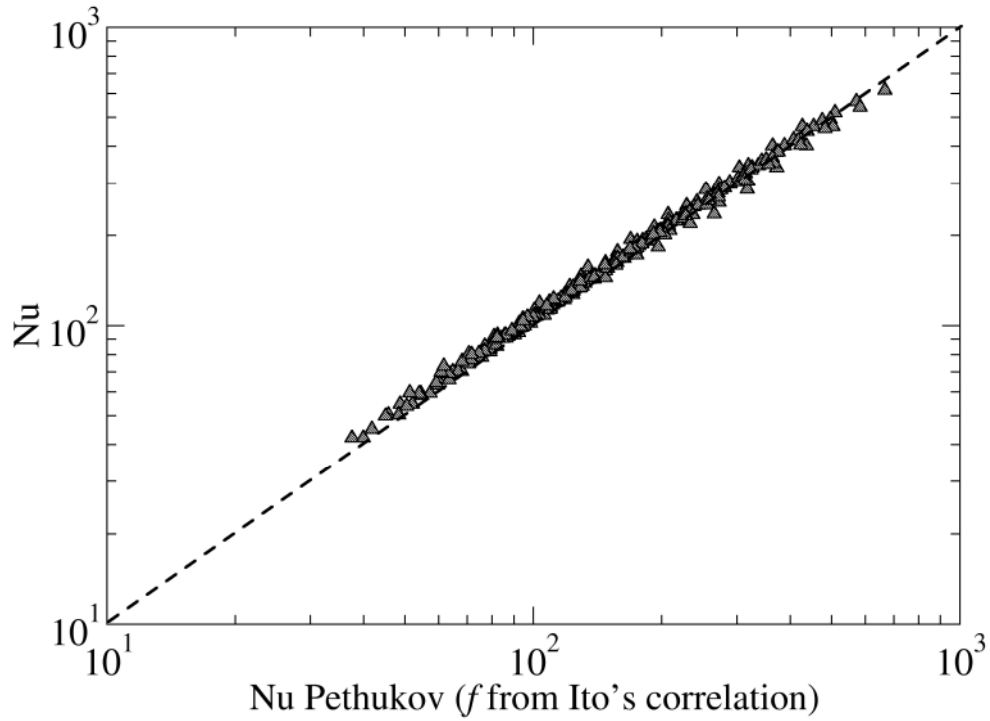


Fig. 20 Parity plot of the mean Nusselt number computed by CFD using the RSM- $\omega$  turbulence model against that predicted by the Pethukov analogy using the values of  $f$  given by the Ito correlation.

Rapporto preparato nel mese di Novembre 2009